small methods
www.small-methods.com

Catalytic Pollutant Upgrading to Dual-Asymmetric MnO_2@polymer Nanotubes as Self-Propelled and Controlled Micromotors for H_2O_2 Decomposition

Yangyang Yang, Kunsheng Hu, Zhong-Shuai Zhu, Yu Yao, Panpan Zhang, Peng Zhou, Pengwei Huo, Xiaoguang Duan, Hongqi Sun, and Shaobin Wang**

Industrial and disinfection wastewater typically contains high levels of organic pollutants and residue hydrogen peroxide, which have caused environmental concerns. In this work, dual-asymmetric MnO_2@polymer microreactors are synthesized via pollutant polymerization for self-driven and controlled H_2O_2 decomposition. A hollow and asymmetric MnO_2 nanotube is derived from MnO_2 nanorods by selective acid etching and then coated by a polymeric layer from an aqueous phenolic pollutant via catalytic peroxymonosulfate (PMS)-induced polymerization. The evolution of particle-like polymers is controlled by solution pH, molar ratios of PMS/phenol, and reaction duration. The polymer-covered MnO_2 tubing-structured micromotors presented a controlled motion velocity, due to the reverse torque driven by the O_2 bubbles from H_2O_2 decomposition in the inner tunnels. In addition, the partially coated polymeric layer can regulate the exposure and population of Mn active sites to control the H_2O_2 decomposition rate, thus avoiding violent motions and massive heat caused by vigorous H_2O_2 decomposition. The microreactors can maintain the function of mobility in an ultra-low H_2O_2 environment (<0.31 wt.%). This work provides a new strategy for the transformation of micropollutants to functional polymer-based microreactors for safe and controlled hydrogen peroxide decomposition for environmental remediation.

1. Introduction

Artificial micro-/nano-reactors with autonomous motion can convert energy/chemicals into a mechanical force, which have been applied in diverse applications ranging from environmental purification to biomedical therapy.[1] Different stimuli (e.g., chemical fuels and other external physical fields) can be activated by H_2O_2-, light-, magnet-, or acoustic wave-sensitive materials and induce passive propulsion in various solutions.[2] Due to the low price, high activity, and structure flexibility, manganese oxide (MnO_2) can efficiently decompose H_2O_2 to generate O_2 bubbles, endowing the asymmetric microreactors with a powerful driving force.[1b] The asymmetric structure was built with four geometries, including sphere-dimer, Janus, hollow, and intrinsic asymmetry.[3] Particularly, developing an inherent asymmetry of one single component can well control the motion behaviors, but remain challenging.

Y. Yang, P. Huo
Institute of Green Chemistry and Chemical Technology
School of Chemistry & Chemical Engineering
Jiangsu University
Zhenjiang 212013, China

Y. Yang, K. Hu, Z.-S. Zhu, Y. Yao, X. Duan, S. Wang
School of Chemical Engineering
The University of Adelaide
Adelaide, SA 5005, Australia
E-mail: xiaoguang.duan@adelaide.edu.au;
shaobin.wang@adelaide.edu.au

P. Zhang
School of Material Science and Engineering
Jiangsu University
Zhenjiang 212013, China

P. Zhou
College of Architecture and Environment
Sichuan University
Chengdu 610065, China

H. Sun
School of Science
Edith Cowan University
Joondalup, WA 6027, Australia

The ORCID identification number(s) for the author(s) of this article can be found under https://doi.org/10.1002/smtd.202300588

DOI: 10.1002/smtd.202300588

For instance, light-driven single-component $BiVO_4$ microreactors were synthesized by a hydrothermal method.[4] The star-shaped $BiVO_4$ microreactors swam in different solutions because of the asymmetrical structure and catalytic surface. The individual $BiVO_4$ as an independent microreactor can capture and kill yeast cells. In addition, symmetrical particles can also aggregate into asymmetrical microreactors. For example, aggregation with different individual Fe^0 nanoparticles would rebuild a larger irregular particle, which fulfilled the degradation of an azo dye with H_2-prepelled motion in citric acid solutions.[5] Thus, homogenous microreactors can be easily prepared by a feasible synthesis strategy but with a noncontrollable structure.

An advanced oxidation process (AOP) is a conventional technique to purify wastewater via the complete mineralization of organic contaminants into CO_2.[6] Notably, the polymerization of micropollutants into solid-state polymers rather than deep oxidation is more appealing in persulfate-based AOPs (PS-AOPs) because of the dramatically reduced chemical input (<1/10) and realizing pollutant carbon recycling and upgrading.[7] For instance, Co_3O_4 with different facets was coated by insoluble polymers derived from a soluble phenolic pollutant through peroxydisulfate (PDS) activation.[7a] In addition, other transitional metal oxides (e.g., NiO[7b] and CuO[7c,d]) can also bond with persulfate (PS) and form a metal-PS complex to convert organics into solid-state polymers via a series of electron transfer, hydrogen abstraction, and cross-linking reactions.

Recently, our group found that the polymerization pathways were regulated by the crystal structure and valence states of MnO_x. Such a process would assemble polymer particles onto the MnO_2 surfaces.[7e] Inspired by this work, we propose that PS-AOPs can be leveraged for advanced material synthesis and functionalization to fulfill different tasks in environmental remediation.[8] Additionally, during the COVID-19 pandemic, large volumes of H_2O_2 have been consumed for a diversity of sterilization and disinfection applications. However, the rapid removal of remaining H_2O_2 by heterogeneous catalysts in pharmaceutical and hospital/clinic wastewater is challenging. Conventional FeO_x and carbon catalysts are low efficiency of H_2O_2 decomposition and will generate large amounts of free radicals that may damage the equipment and lead to disinfection byproducts.[9] In the contrary, H_2O_2 decomposition by MnO_x is vigorous and uncontrollable, spontaneously generating massive heat and oxygen to induce a potential hazard.

In this work, we prepared MnO_2 tubular microreactors by selective acid etching to realize internal asymmetry with a hollow tubular structure. On this basis, we constructed a dual-asymmetric structure via surface modification with polymers through PS-AOP, leveraging phenolic micropollutants as the monomer. The derived MnO_2@polymer microreactors were applied for self-moving and controlled H_2O_2 decomposition in water. The evolution of MnO_2 to MnO_2@polymer nanotubes was systematically investigated by scanning electron microscopy (SEM) and scanning transmission electron microscopy (STEM). Especially, we applied in situ Raman spectroscopy, stoichiometric analysis, X-ray photoelectron spectroscopy (XPS), and quenching experiments to reveal the polymerization of phenolics into polymers with ultralow chemical input. For the first time, we used nonradical persulfate chemistry as an innovative and controlled polymer coating approach to obtain a functional polymer layer from phenolic wastewater onto the MnO_2 surface. We will manipulate the thickness of the coating layer to further regulate the H_2O_2 decomposition rate and efficiency. This work provides a novel application of persulfate nonradical chemistry to convert phenolic pollutants and tubular MnO_2 into self-propelled functional catalysts for controlled H_2O_2 elimination and water decontamination spontaneously.

2. Results and Discussion

2.1. Design and Synthesis of MnO_2@polymer Nanotubes

As an H_2O_2-propelled microreactor, an asymmetric structure is built by uneven H_2O_2-sensitive active materials to generate O_2 bubbles to swim in the solution. In this work, we prepared a single-component tetragonal α-MnO_2 with asymmetric shapes via a facile hydrothermal method, as shown in **Figure 1**a–g. Notably, MnO_2 at 2 h is composed of nanorods and laminar flowers (Figure S1, Supplementary Information). Thus, the structure of MnO_2 reconstructed from layers to nanorods at above 2.5 h. Through selective HCl etching on the tetragonal (001) surface,[10] MnO_2 nanorods are converted into nanotubes during the aging period from 2 to 12 h (Figure 1a–e). MnO_2 obtained at 12 h is denoted as MnO_2-0.5. Specifically, the propeller-like MnO_2-0.5 nanotubes are built by a dominant nanotube with several tubular tails (Figure 1f and Figure S2, Supplementary Information). Generally, MnO_2 can be used to degrade toxic organics via peroxymonosulfate-based AOPs (PMS-AOPs).[11] In this work, 100% of phenol was oxidized and converted by activated PMS into polymer particles accumulated on the surface of MnO_2-0.5 nanotubes (Figure 1h,i, Figure S3, Supplementary Information).

The deposited polymeric particles are highly stable and will not dissolve in water and methanol solutions. As reported in our previous work, the particle was polyphenol generated via a cross-linking process.[7e] The polymer-coated MnO_2-0.5 nanotube was denoted as MnO_2@polymer-0.5. In **Figure 2**a, MnO_2@polymer-0.5 nanotubes owned an inner "V" tunnel due to the selective acid etching, assembling into a dual-asymmetric structure with an outside propeller and an inside tunnel. TEM images of MnO_2@polymer-0.5 show that the polymer particles assembled into one layer and covered MnO_2 surface (Figure 2b). Also, the fast Fourier transform (FFT) images, XRD pattern, and EDS spectra confirm that the particles were composed of carbon and oxygen with an amorphous structure (Figure 2b3,b6 and Figures S4, and S5, Supplementary Information). Therefore, PMS-AOPs can be applied for in situ synthesizing polymeric functional materials via catalytic transformation of aqueous micropollutants (e.g., phenol).

As demonstrated in Figure S6a, Supplementary Information, the catalytic phenol oxidation decreased with the rise of phenol loadings (0.2–1.0 mM) in simulated wastewater. Simultaneously, the surface of MnO_2-0.5 nanotubes was covered by more particle-like polymers (Figure S6b–e). Thus, 1.0 mM phenol was selected to investigate the effect of catalyst concentration. In Figure S7a, Supplementary Information, more phenol was degraded with the increase of MnO_2 because more Mn active sites were introduced for PMS activation. Moreover, larger particles were coated on the MnO_2 surfaces (Figure S7b–e, Supplementary Information), indicating that the size of the particles became bigger at

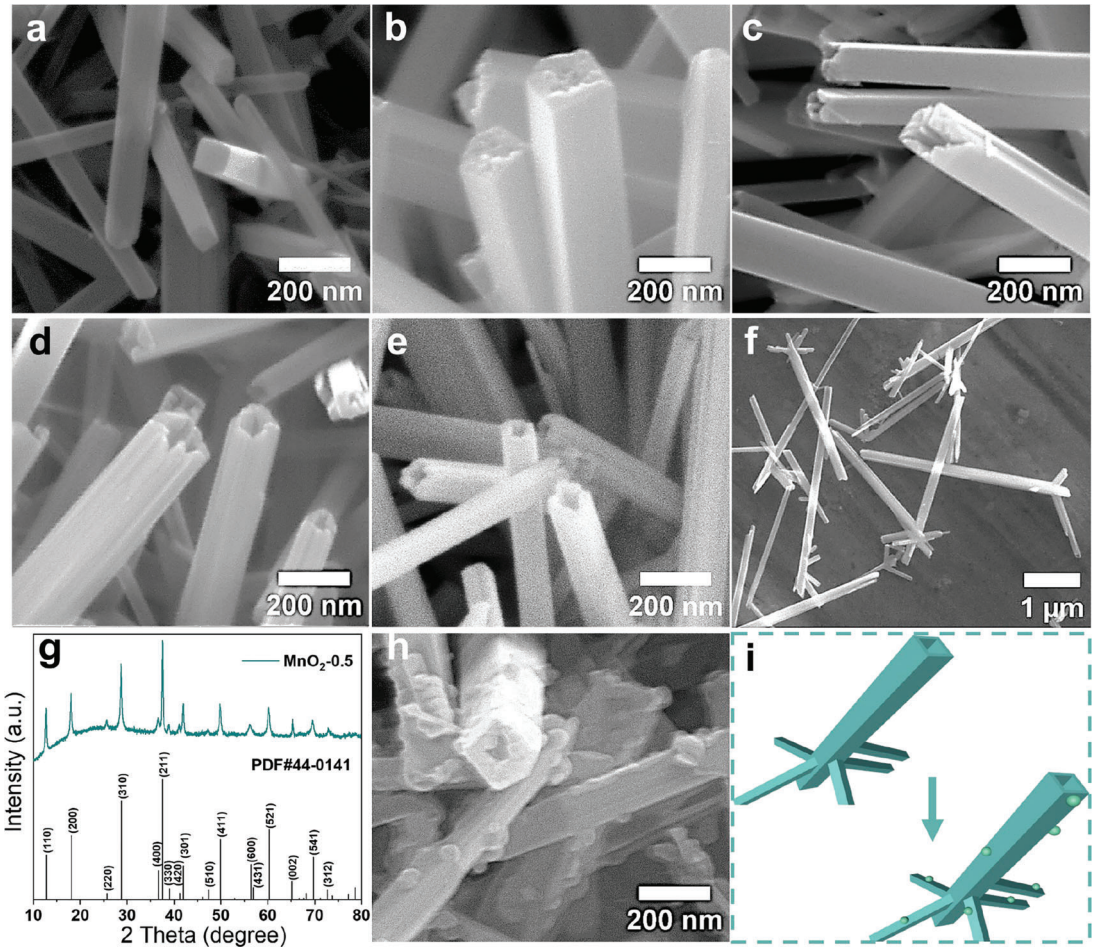

Figure 1. SEM images of MnO_2 nanorods or nanotubes obtained at different reaction time. a) 2 h, b) 2.5 h, c) 3 h, d) 5 h, and e,f) 12 h; g) XRD pattern of MnO_2-0.5 nanotubes; h) SEM image of MnO_2-0.5 nanotubes after polymerization reaction; i) Schematic graph of MnO_2-0.5 nanotubes after reaction with phenol. Experimental conditions: $[phenol]_0 = 0.2$ mM, $[MnO_2\text{-}0.5]_0 = 0.3$ g L^{-1}, $[PMS]_0 = 0.4$ mM, T = 25 °C, pH = 7.0, and reaction time = 60 min.

a higher reaction rate of phenol oxidation. To obtain a uniform polymeric coating, 0.2 g L^{-1} MnO_2-0.5 nanotubes were used in further experiments. Then, we investigated the changes in the coating layer at various aging periods. Figure 2c–f, Figures S8, and S9, Supplementary Information, show that particle-like polymers increased to 10.0, 15.4, 21.6, and 24.7 wt.% at different reaction durations (5, 15, 60, and 120 min, respectively). Nearly 100% MnO_2 nanotubes were coated by polymers. The black MnO_2-0.5 powders turned into gray MnO_2@polymer-0.5 due to the coating of a yellow polymer layer (Figure S10, Supplementary Information). The crystal structure of MnO_2 remained the same after the polymerization reaction (Figure S11, Supplementary Information). Figure 2c1–f2 presents that the inner and outer surfaces of MnO_2-0.5 nanotubes were covered by a polymeric layer with ≈30 nm thickness, which was likely due to the interfacial reactions between MnO_2 and phenol.

2.2. Synthetic Mechanism of Polymeric Layers

To clarify the evolution mechanism of polymers, we systematically studied the reaction process in the PMS/MnO_2 system. In this work, we carried out two steps to synthesize the MnO_2@polymer composite. First, phenol and MnO_2 were stirred in a water solution for 30 min, denoted as the Mn-induced polymerization (Mn-Poly) stage. Second, PMS was added to the mixed solution with stirring for different durations. This process is a PMS-induced polymerization (PMS-Poly) stage. In the step of Mn-Poly, some smaller particles were attached to the MnO_2 surfaces (Figure S12, Supplementary Information). With the increase of solution pH (below 10), MnO_2 surface was coated with more particles. Then at solution pH 11, MnO_2@polymer displayed fewer deposited polymer particles. In this process, high-valence metal ($Mn^{IV}_{(s)}$) dominated the oxidation and polymerization of phenol into phenolic polymers.[7e,12] Specifically, phenol was converted into phenoxy radicals induced by $Mn^{IV}_{(s)}$ via a proton-coupled electron transfer (PCET) that involved one-H-atom-abstraction and one-electron-oxidation.[13] Then partial monomer radicals will polymerize into phenolic polymers, accumulating on the MnO_2 surface. Notably, solution pH near p*K*a of phenol (9.98) achieved the highest performance of phenol polymerization due to the heterolytic hydrogen bond cleavage via the PCET process.[7d,13]

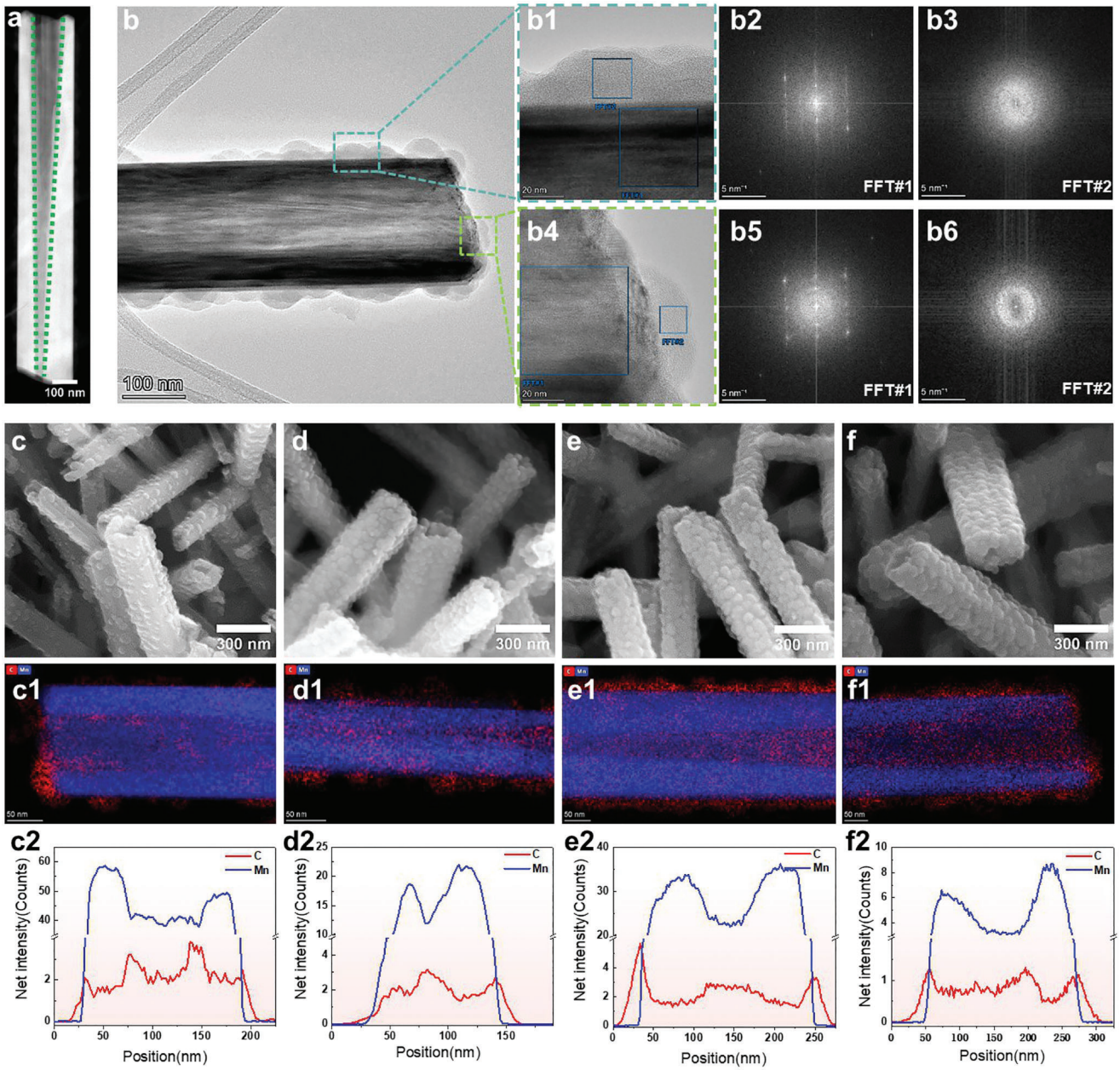

Figure 2. a) A STEM image of individual MnO_2@polymer-0.5 nanotube without outside propeller; b-b6) TEM images of MnO_2@polymer-0.5 nanotubes with fast Fourier transform (FFT) images; SEM images with EDS mapping analysis of MnO_2@polymer-0.5 nanotubes and EELS analysis of Mn and C for the whole image at different reaction time: c-c2) 5 min, d-d2) 15 min, e-e2) 60 min, and f-f2) 120 min.

However, in the PMS-Poly stage, fewer polymer particles were produced on the surface of MnO_2 nanotubes when solution pH was above 9, resulted from the prohibited degradation efficiency due to the less reactive alkaline-activated PMS (Figure S13e–g and Figure S14b, Supplementary Information).[14] With the increase in solution pH (5–8), MnO_2 attained a more phenol removal (Figure S14a, Supplementary Information), and the polymeric particles became larger, indicating that the size of particles exhibits a positive correlation with the phenol removal rate (Figure S13, Supplementary Information). Thus, we kept the solution at neutral pH of 7 to analyze polymeric initiators in the process of PMS-Poly. Notably, MnO_2 can activate PMS to form various reactive oxygen species (ROS), including high-valence Mn species ($Mn^{IV}_{(s)}$),[15] free radicals ($SO_4^{\bullet-}$,•OH, and $O_2^{\bullet-}$),[11] singlet oxygen ($^1O_2$),[11] and Mn-activated persulfate complexes.[7e]

To investigate the possible ROS (e.g., $SO_4^{\bullet-}$, •OH, $O_2^{\bullet-}$, and $^1O_2$), we applied various quenchers in the MnO_2/PMS system. We used ethanol (EtOH), tert-butanol (TBA), and chloroform to respectively identify the contributions of ($SO_4^{\bullet-}$ and •OH), •OH, and $O_2^{\bullet-}$ radical species in the AOPs systems.[16] In addition, 2,2,6,6,-tetramethyl-4-piperidinol (TEMP) was selected to probe and estimate the non-radical species ($^1O_2$).[17] **Figure 3**a shows

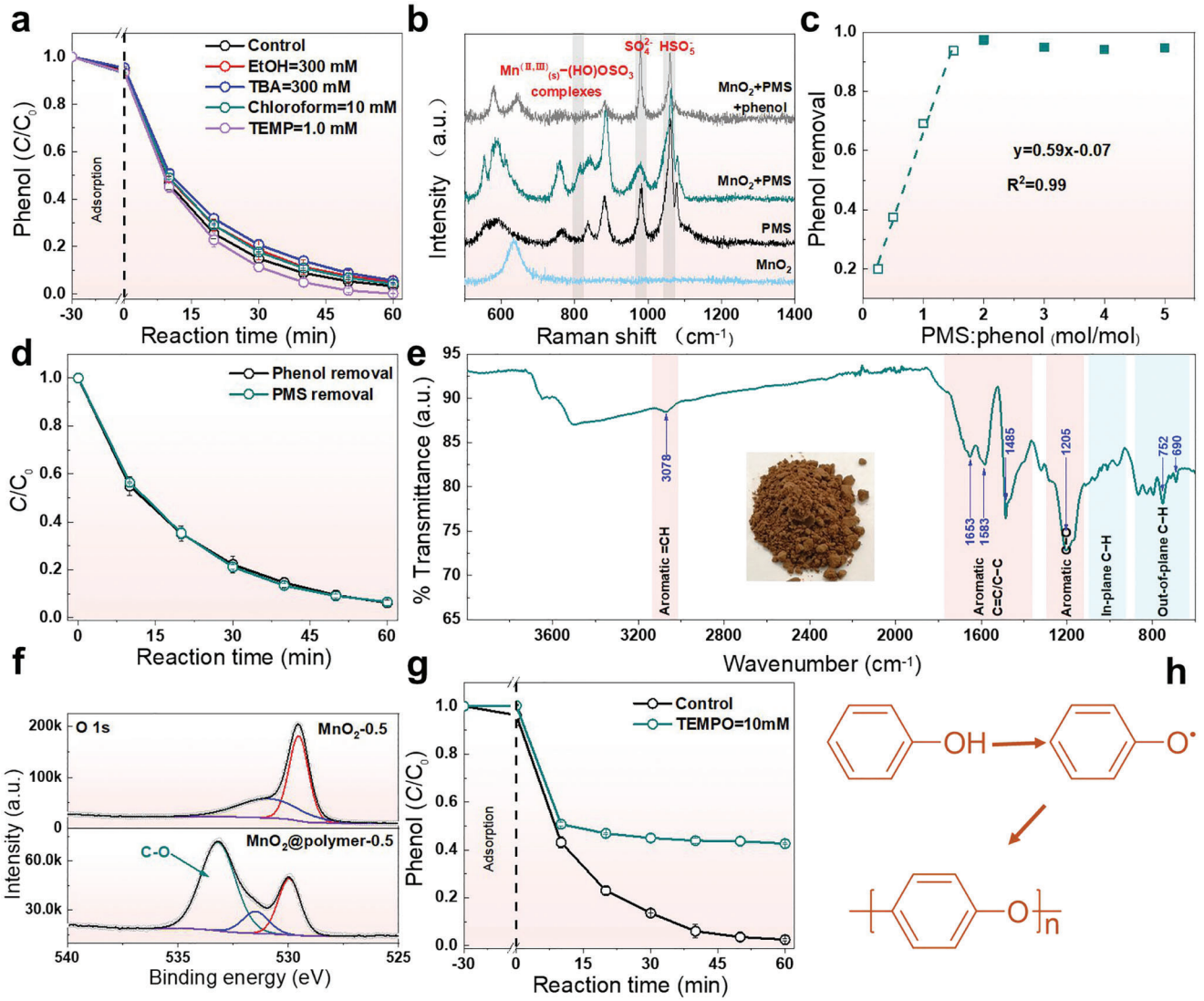

Figure 3. a) Catalytic performance of phenol oxidation with the presence of various quenchers; b) in situ Raman spectra of MnO_2-0.5 nanotubes in PMS + phenol solution; c) fitting line between phenol removal and the molar ratio of PMS to phenol; d) phenol and PMS removals during the reaction at a molar ratio of 1.5 (PMS:phenol); e) FTIR spectra of polymers; f) XPS spectra (O 1s) of MnO_2-0.5 and MnO_2@polymer-0.5 nanotubes; g) quenching performance in the presence of TEMPO; h) schematic polymerization reaction. Experimental conditions: $[phenol]_0$ = 0.2 mM, $[MnO_2\text{-}0.5]_0$ = 0.3 g L^{-1}, $[PMS]_0$ = 0.4 mM, T = 25 °C, pH = 7.0, and reaction time = 60 min.

the effects of quencher additions on phenol oxidation in PMS-AOP systems. Phenol degradation experienced a slight variation with the presence of all quenchers and exhibited a weak signal of $O_2^{\bullet-}$ (Figure S15, Supplementary Information), indicating the negligible contribution of the free radicals and singlet oxygen.

Then, we used in situ Raman spectra to detect the Mn-activated persulfate complexes in the step of AOPs (Figure 3b). After adding PMS in the MnO_2 solution, a new peak (815 cm^{-1}) appeared for $Mn^{(II,III)}{}_{(s)}$−$(HO)OSO_3^-$ (MnO_2−PMS) complexes, which was assigned to the bonding signal between MnO_2 and PMS.[7e,18] Afterwards, the peak disappeared in the presence of phenol. Simultaneously, the peak intensity of HSO_5^- decreased with an increase of SO_4^{2-} peak, indicating that the MnO_2−PMS complex would react with phenol and transform into SO_4^{2-}; meanwhile, phenol was polymerized into phenolic polymers. In addition, an ionic strength analysis illustrates that the effect of phenol oxidation decreased slightly with a rise in $NaClO_4$ concentration (10–100 mM, Figure S16, Supplementary Information). This resulted from the weakened inner-sphere interactions (via covalent or ionic bonding) between PMS and MnO_2 due to the reduced zeta potential of MnO_2 nanotubes at a higher concentration of $NaClO_4$ (Figure S17, Supplementary Information).[19] Thus, the MnO_2−PMS complex was the main ROS in phenol degradation via AOPs. In addition, in situ open potential of MnO_2-0.5 nanotubes shows a sharp drop upon phenol addition, suggesting that the direct electron-transfer process between MnO_2−PMS complex and phenol-dominated phenol oxidation in the PMS/MnO_2 system (Figure S18, Supplementary Information).

Then we estimated the stoichiometric ratio between PMS and phenol in the system of phenol + PMS + MnO_2. Figure 3c and Figure S19, Supplementary Information, demonstrated that phenol removal increased from 20% to 97% with an increased molar ratio of PMS:phenol (0.25–2.0) in the presence of sufficient Mn active sites. Afterward, phenol oxidation reached equilibrium (95%). The phenol removal and molar ratio are fitted into a linear relation with a slope value of 0.59; that is, one molar phenol molecule consumes about 1.7 mole PMS molecules in the presence of sufficient catalysts. Figure 3d shows that phenol was completely converted by PMS at a molar ratio of 1.5. As a result, an excessive PMS input did not enhance phenol degradation but caused a slightly declined removal due to occupying phenol adsorption sites, which might further decrease the thickness of coated polymers.

Recently, phenolic polymers were synthesized by different transitional metal oxides via PS activation, where the process of polymerization was varied in different systems.[7,20] For instance, phenolics were initiated into phenoxy radicals via a PCET reaction by CuO–PDS complexes. Then the phenoxy radicals acted as monomers and generated polymers via coupling and cross-linking reactions.[7d] However, in Co_3O_4/PMS systems, phenol is transferred into phenoxonium ion monomers and polymerized into phenolic polymers.[20] Further, we analyzed the structure and polymerization process of the obtained polymers. Figure S20, Supplementary Information, presents the SEM images of polymers after HCl etching. Several polymeric nanotubes collapsed into small particles, probably due to the weak mechanical properties of the polymers. Figure 3e shows the FTIR spectra of the polymers. After the polymerization reaction, the benzene ring of phenol was retained without a hydroxyl group. The peak at 1205 cm^{-1} was ascribed to aromatic C–O, indicating H-abstraction by MnO_2–PMS complexes.[21] The bond of C–O also can be confirmed by XPS spectra (Figure 3f and Figure S21, Supplementary Information). Thus, the main structure of the polymer was composed of benzene rings linked with oxygen.

We further performed the quenching experiments and nucleophilic analysis to confirm the monomer during the polymerization reaction. 2,2,6,6-Tetramethyl-1-piperidinyloxy (TEMPO) and butylated hydroxyl toluene (BHT) have been widely applied to scavenge organic radicals (*R*•) to estimate the presence of *R*•.[22] Figure 3g presents the effect of phenol oxidation with the TEMPO addition. The phenol removal decreased from 97% to 57% after adding 10 mM TEMPO. A similar result was also found with the presence of BHT (Figure S22, Supplementary Information). These indicated that R• dominated the polymerization step of AOPs (Figure 3h). In addition, nucleophilic reagents (e.g., acetonitrile and methanol) can scavenge phenoxonium ions and inhibit the polymerization of phenol.[20] Figure S23, Supplementary Information, shows that phenol degradation decreased with the raised volume ratios of nucleophilic reagents:water from 0:1 to 1:0, which is likely due to the scavenging of phenoxonium ions. Thus, the organic solvent was mainly responsible for inhibiting the interaction between MnO_2 and PMS rather than acting as a nucleophilic reagent. This was due to the better wettability and lower solubility of the organic solvent than water, thus prohibiting phenol degradation in the water/nucleophilic reagent solutions. As a result, phenol was initially transferred into phenoxy radicals (Equation 1) and then polymerized into phenolic polymers, as illustrated in Figure 3h.

$$C_6H_5OH + HSO_5^- + OH^- \rightarrow [C_6H_4O] + 2\,H_2O + SO_4^{2-} \quad (1)$$

Figure 3c shows that one molar phenol would consume 1.7 moles of PMS (PMS/phenol = 1.7). As demonstrated in Figure 3b, PMS would bond with MnO_2 and form a $Mn^{(II,III)}{}_{(s)}$–$(HO)OSO_3^-$ complex to oxidize phenol via a direct electron-transfer process. Thus, PMS would receive electrons from both outer phenol and inner MnO_2 as follows, giving rise to higher PMS consumption.[7e]

$$Mn^{II}_{(s)} - (HO)\,OSO_3^- + 2e \rightarrow Mn^{III}_{(s)} + SO_4^{2-} + OH^- \quad (2)$$

$$Mn^{III}_{(s)} - (HO)\,OSO_3^- + 2e \rightarrow Mn^{IV}_{(s)} + SO_4^{2-} + OH^- \quad (3)$$

The surface $Mn^{IV}{}_{(s)}$ increased from 52.4% to 78.9% after the reaction (Figure S24, Supporting Information). The Mn average oxidation state (AOS) of MnO_2 decreased from 3.5 to 3.4 based on the following equation: AOS = 8.92-1.13Δ.[23] Oxidized by the nonradical PMS complex and Mn active sites on the MnO_2 surface, phenol was converted into phenoxy radicals, which acted as monomers to generate phenolic polymers via coupling and cross-linking reactions over the MnO_2 surface.

Figure 4 summarizes the generation of MnO_2@polymer nanotubes and the growth mechanism of particle-like polymers. Two steps induced the growth evolution of polymers, including Mn-Poly and PMS-Poly. Smaller and less polymeric particles were attached to the surface of dual-asymmetric MnO_2 nanotubes during the Mn-Poly process. In the subsequent step of PMS-Poly, massive particles were coated on the outer surface of MnO_2, and less phenolic polymers were located on the inner surface due to the limited mass transfer and thus a lower polymerization rate. Generally, free radical polymerization follows three steps: 1) initiation, where the R is converted into active R• by initiators; 2) propagation, where the R• acts as a monomer to pair off other R•, increasing polymerization degree via a coupling reaction; 3) termination, where the growth process is inhibited by the destruction of monomers or the lack of initiators.[24]

In the two steps of Mn-Poly and PMS-Poly in the system of (phenol + PMS + MnO_2), $Mn^{(IV)}{}_{(s)}$ species and $Mn^{(II,III)}{}_{(s)}$–$(HO)OSO_3^-$ complexes were the initiators in the polymerization of phenol, respectively. The initiators would induce one-H-atom-abstraction and one-electron-oxidation reactions via a PCET process, generating phenoxy radicals to polymerize into polyphenols. The polymerization reaction would be terminated by the lack of Mn initiators because of the complete coating of the MnO_2 surface by polymers. Thus, the polymer evolution processes can be regulated by the dosages of three reactants (e.g., phenol, PMS, and MnO_2) and solution pH to attain a controlled reaction rate. Specifically, due to the interfacial reaction between MnO_2 and phenol, the polymerization reaction would be inhibited after the coating of polymers. This would lead to only one polymeric layer on MnO_2 surfaces (Figure 2b). Higher loadings of reactants (PMS and MnO_2) would enhance the polymerization reaction, further enlarging the size of polymer particles (Figure S6 and S7, Supporting Information) and thickening the coating layers. In addition, solution pH near the p*K*a

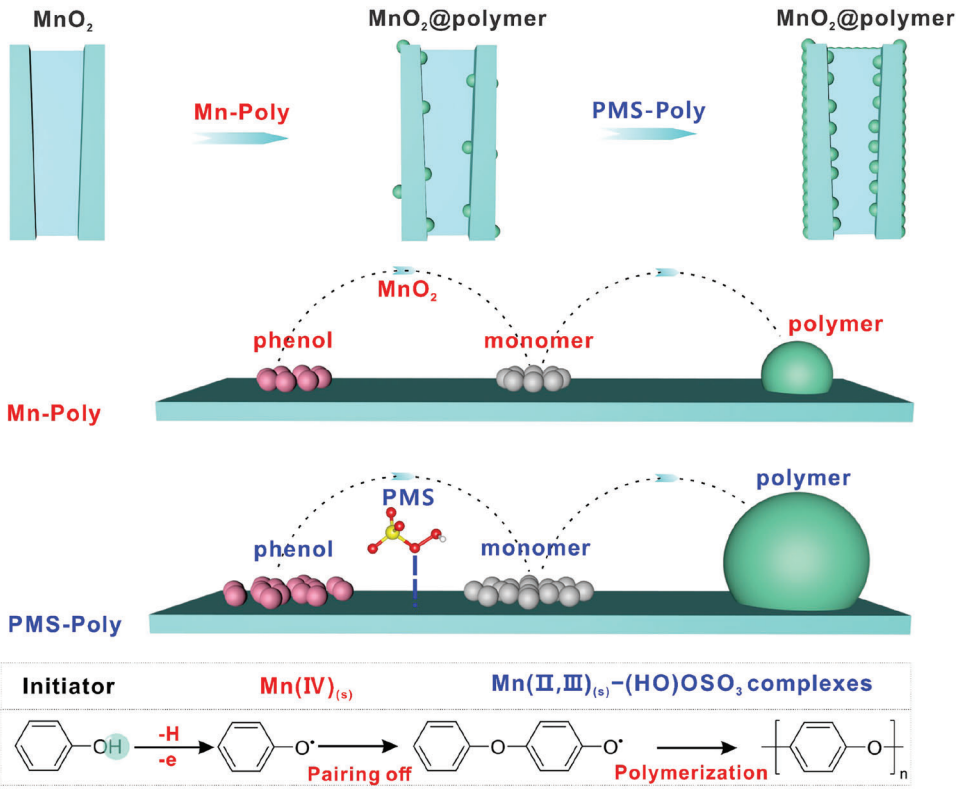

Figure 4. The proposed evolution process of MnO_2@polymer nanotubes.

value of organics accelerated the H-abstraction during the PCET process, which also could increase the particle sizes of the polymers (Figure S13, Supporting Information). Then the modified MnO_2@polymer nanotubes were applied to H_2O_2 decomposition with different coverage percentage and thickness.

2.3. Evaluation of H_2O_2 Decomposition by Self-Propelled Microreactors

H_2O_2, as a strong oxidant, is widely used in industrial manufacturing (e.g., textile and paper production) and sterilization (e.g., disinfectants and deodorants).[9] High-concentration H_2O_2 cannot be rapidly removed by heat or light (Figure S25, Supporting Information). Furthermore, stabilizers (e.g., sodium silicate and magnesium silicate) are typically added to reduce its spontaneous decomposition, leading to massive stable H_2O_2 with the stabilizers presented in industrial and disinfection wastewater.[9] MnO_2 is a low-cost and highly active catalyst that can directly decompose the remaining H_2O_2 into water and O_2 (**Figure 5**a-I).[25] In addition, H_2O_2 is the fuel to propel the motion of Mn-based microreactors in solutions, using the decomposed O_2 as a torque.[1b] Thus, MnO_2-based microreactors with a micro-mixing torque can be a catalyst to remove H_2O_2 without a mechanical energy input. Generally, 3 wt.% H_2O_2 is used for general disinfection purposes, such as in surface disinfection, food processing, or healthcare settings. In this work, we adopted even lower concentrations (1 wt.%-333 mM or 0.3 wt.%-100 mM) to simulate the residue H_2O_2 in wastewater.

In this work, we mainly proposed two strategies to control H_2O_2 decomposition. 1) Single-asymmetric MnO_2 nanorods with propeller-like tails were gradually etched into dual-asymmetric MnO_2 nanotubes with an inner "V" tunnel via a hydrothermal method (Figure 5a-II); 2) Tubular MnO_2 was partially coated by particle-like phenolic polymers through PMS-AOPs, giving rise to MnO_2@polymer nanotubes (Figure 5a-III). The mobility of MnO_2-based microreactors was examined by an optical microscope with an inverted camera in 1 wt.% H_2O_2 solution. First, we detected the mean velocity of MnO_2 at different time in Figure 5b. With the rise of aging time, the speed reduced from 39 to 13 μm s^{-1} at 2.5–12 h (Video S1, Supporting Information). On the contrary, MnO_2 nanotubes at 12 h (MnO_2-0.5) decomposed more H_2O_2 with a slower motion behavior (Figure 5c and Figure S26, Supporting Information).

Specifically, we proposed two modes of oxygen formation for MnO_2 nanorods and nanotubes in Figure S27, Supporting Information. MnO_2 nanorods generate more oxygen at the bottom of the tails, inducing a powerful torque to propel rod-like microreactors (Figure S27a, Supporting Information). After HCl etching, the inner "V" type of tunnel catalytically decomposed more H_2O_2 and produced more oxygen from the inner structure, providing a reverse torque to inhibit the directional mobility in the solution (Figure S27b, Supporting Information). This would reduce the speed of tubular microreactors. Therefore, the performance of H_2O_2 decomposition was tailored through the modification from single-asymmetric nanorods to dual-asymmetric nanotubes. Further, we used PMS-AOPs to partially endow MnO_2 nanotubes with a polymeric layer assembled by particle-like polymers on the

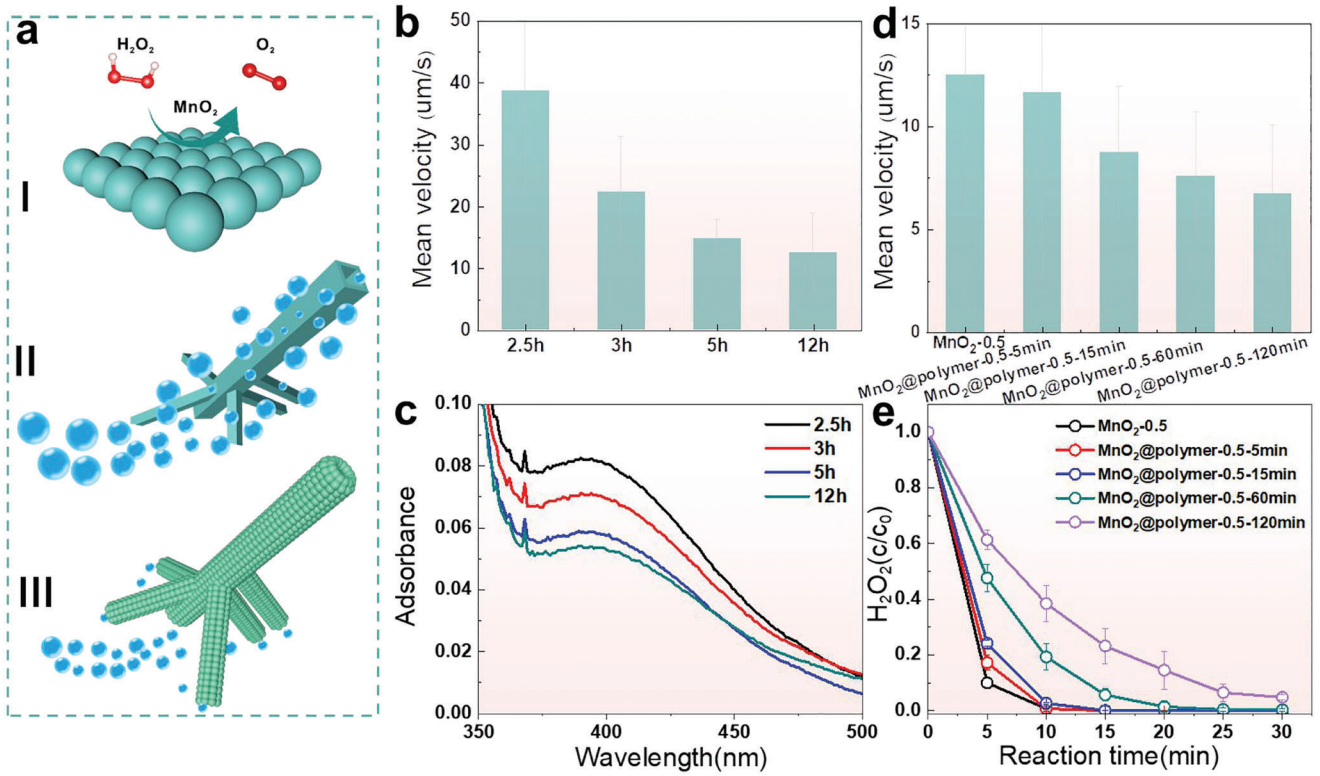

Figure 5. a) Schematic graph of H_2O_2 decomposition by MnO_2 and MnO_2@polymer; b) mean velocity of MnO_2 microreactors at different reaction time in 1 wt.% of H_2O_2 solution; c) ultraviolet-visible (UV-vis) absorption spectra of H_2O_2 solution with 390 nm at 5 min; d) mean velocity of MnO_2@polymer microreactors at different reaction time in 1 wt.% of H_2O_2 solution; e) catalytic performance of H_2O_2 decomposition by MnO_2@polymer microreactors at different reaction time. Experimental conditions: $[catalysts]_0 = 0.2$ g L^{-1}, $[H_2O_2]_0 = 100$ mM, T = 20 °C, and reaction time = 30 min.

MnO_2 surfaces, deriving MnO_2@polymer nanotubes. Figure 5d presents that the tubular MnO_2@polymer microreactors swam more slowly with the increase in the aging duration through covering more Mn active sites by the polymer (Video S2, Supporting Information), which resulted in the declined performance of H_2O_2 decomposition (Figure 5e). Due to the excessive coating layer on MnO_2 nanotubes at 120 min, less than 50% of MnO_2@polymer-0.5–120 min microreactors could swim in the H_2O_2 solution. Thus, the H_2O_2 decomposition was controlled through partially covering surface Mn sites by the polymeric particles, limiting surface H_2O_2 adsorption/degradation kinetics. Also, the H_2O_2 removal rate can be regulated by the loading of MnO_2@polymer microreactors, and a higher dosage of microreactors accelerated H_2O_2 decomposition (Figure S28, Supporting Information).

In addition, dual-asymmetric MnO_2 nanotubes with different specific surface areas (SSAs) were synthesized by adjusting the concentration of hydrochloric acid (0.9, 1.3, and 1.5 mL) to regulate the H_2O_2 decomposition. Figure S29, Supporting Information, presents the SEM images of tubular MnO_2-0.9, MnO_2-1.3, and MnO_2-1.5. With the increase of HCl dosage, the wall of nanotubes became thinner gradually but maintained the crystal structures (Figure S30, Supporting Information), giving rise to enlarged SSAs from 20 to 31 m^2 g^{-1} (Figure S31, Supporting Information). Similar to the MnO_2-0.5 nanotubes, small polymer particles were attached to the surfaces of tubular MnO_2-(0.9, 1.3, and 1.5) in Figure S32a–c. The phenol oxidation enhanced with the increase of HCl loadings (Figure S32d, Supporting Information), due to the increased SSAs of MnO_2 nanotubes (Figure S31, Supporting Information). Moreover, a higher phenol loading would induce more polymeric particles (27.6, 28.0, and 30.7 wt%) coated on the surfaces of MnO_2-(0.9, 1.3, and 1.5) (Figure S33–S34, Supporting Information). Figure S35, Supporting Information, presents the performance of H_2O_2 decomposition by the different MnO_2@polymer nanotubes. MnO^2@polymer-0.9 and MnO_2@polymer-1.3 decomposed 88% of H_2O_2, slightly lower than that of MnO_2@polymer-1.5 (92%), which was likely due to the higher velocity (Figure S36 and Video S3, Supporting Information) and a higher SSA (Figure S31, Supporting Information) of MnO_2@polymer-1.5 microreactors. Thus, controlling the size of MnO_2 nanotubes in the composites can regulate the H_2O_2 decomposition rate. In summary, conventional PS-AOPs can act as an in situ synthetic method for coating polymers onto MnO_2 to obtain surface functionalization. Meanwhile, the hazardous organics (phenol, as the polymer precursor) are simultaneously removed from aqueous solutions. The morphology and structure asymmetry of the nanoreactor offers optimal H_2O_2 decomposition rate and sustained motion in water without extra chemical and mechanical energy input.

3. Conclusion

In this work, we implemented a new strategy of phenolic pollutant adsorption and oxidative polymerization for

designing a dual-asymmetric MnO_2 nanotube converted from single-asymmetric MnO_2 nanorods by selective acid etching and partially polymeric coating. The polymerization reaction was achieved from nonradical phenol oxidation by $Mn^{(IV)}{}_{(s)}$ and $Mn^{(II,III)}{}_{(s)}$–$(HO)OSO_3^-$ complexes via two steps of Mn-Poly and PMS-Poly, respectively. During the process, phenolic pollutants would lose one H-atom and contribute one electron via a PCET process, generating phenoxy radicals that are further cross-linked into phenolic polymers. Those dual-asymmetric MnO_2 and MnO_2@polymer nanotubes were used as microreactors for self-driven and controlled H_2O_2 decomposition. Their performance of H_2O_2 decomposition was regulated by varying asymmetric structures from nanorods to nanotubes, modified coating degrees, and controlled exposure of Mn active sites. The approach of nonradical AOPs to convert toxic aqueous organics (e.g., phenolics) into solid-state polymers will remarkably reduce peroxide consumption and realize catalytic pollutant upgrading into polymers for manufacturing a controlled and sustainable functional MnO_2@polymer microreactors. The structure and morphology-engineered microreactors are promising to remove H_2O_2 and other contaminants in wastewater in a controlled and sustainable manner. This work demonstrates a feasible technique for the fabrication of intelligent nanomaterials by AOPs from water pollutants and their further application in H_2O_2 control and removal.

4. Experimental Section

Chemicals: Potassium permanganate ($KMnO_4$), hydrochloric acid (HCl, 37 wt.%), OXONE® ($KHSO_5{\cdot}0.5KHSO_4{\cdot}0.5K_2SO_4$, a source of PMS), potassium hydroxide (KOH), sulfuric acid (H_2SO_4), ethanol, tert-butanol (TBA), trichloromethane, 2,2,6,6,-tetramethyl-4-piperidinol (TEMP), 2,2,6,6-tetramethyl-1-piperidinyloxy (TEMPO), butylated hydroxyl toluene (BHT), 5,5-dimethyl-1-pyrroline N-oxide (DMPO), sodium bicarbonate ($NaHCO_3$), potassium iodide (KI), potassium titanium oxide oxalate dehydrate ($C_4K_2O_9Ti{\bullet}2H_2O$), and phenol were purchased from Sigma-Aldrich. All the chemicals are used without further purification and in the experiments milli-Q water (18.2 MΩ cm) was used.

Preparation Procedures: MnO_2 nanorods or nanotubes were synthesized via a modified hydrothermal method.[10] Specifically, 0.45 g $KMnO_4$ was dissolved into 40 mL H_2O. Then 37 wt.% of HCl (0, 0.5, 0.9, 1.3, and 1.5 mL) was added into $KMnO_4$ solution with stirring for 20 min. The mixed solution was transferred into a Teflon-lined autoclave (100 mL) at 140 °C for different durations (2–12 h).

MnO_2@polymer nanotubes were prepared through a conventional batch experiment with pollutant degradation. Different loadings of MnO_2 nanotubes (0.1–0.4 g L^{-1}) were added into 2 L H_2O with ultrasonic treatment for 2 min. Then 0.2–1.0 mM of phenol was dissolved into the solution for 30 min (denoted as the adsorption period). After the adsorption process, different concentrations of PMS (molar ratio of PMS to phenol at 2) were dropped into a mixed solution with different durations (5–120 min). The solution pH (3–11) was adjusted by a pH-stat. The obtained materials were filtered and washed several times with water. Then, the coated MnO_2 nanotubes were dried at 60 °C for 8 h.

Materials Characterizations: Powder X-ray diffraction (XRD) was analyzed by a D8 Advance X-ray diffractometer (Bruker AXS) at 40 kV and 40 mA using Cu Kα radiation (λ = 1.54186 Å). The morphologies were analyzed by scanning electron microscopy (SEM, FEI Quanta 450 FEG). The scanning transmission electron microscopy (STEM) images with energy-dispersive X-ray spectroscopy (EDS) mapping analysis were conducted on a JEOL 2100F microscope. Raman spectroscopy was performed on a Horiba Scientific instrument from Germany at 532 nm. Electron paramagnetic resonance spectra were obtained using a ESR spectrometer (Bruker EMX). The compositions and chemical states of the surface elements were determined by X-ray photoelectron spectroscopy (XPS).

Motion Characterizations: For those tests, a sample solution was put into a dish. The motion behavior was visualized with a 12 mm diameter viewing area using a Nikon Ti E live cell microscope with an inverted camera. Velocity tracking data were collected by the Image J software (Fiji) for the mean velocity from 10 individuals. In the H_2O_2 decomposition analysis, no surfactant was used in all experiments.

Determination of PMS Concentration: The PMS concentration was analyzed by an iodometric method. Typically, a solution sample (0.2 mL) was mixed with 0.06 g $NaHCO_3$, 0.3 g KI, and 2.8 mL H_2O for analysis at 319 nm by UV-vis spectroscopy (Cary Series, Agilent Technologies).

Electrochemical Measurements: An electrochemical workstation (CHI 760E) was employed for the open circuit potential-time tests. A glassy carbon electrode was coated with the catalyst sample (10 mg mL^{-1}) as the working electrode. An Ag/AgCl (saturated KCl) electrode and a Pt wire were employed as the reference and counter electrodes, respectively.

Phenol Degradation Tests: A 200 mL solution was put in a 250 mL beaker with catalyst (0.1–0.4 g L^{-1}), PMS (molar ratio of PMS to phenol at 2), and phenol (0.2–1.0 mM) at a solution pH 7 with a pH-stat. KOH and H_2SO_4 were used to maintain the solution pH. During a set time interval, a solution sample (1 mL) was withdrawn with a polyether sulfone filter (0.22 µm) and injected into 20 µL ethanol in an HPLC vial. The solution samples were separated by a C-18 column and monitored by a UV detector in an ultrahigh performance liquid chromatography (UHPLC, Thermo Scientific).

H_2O_2 Degradation Analysis: A testing system (200 mL) was carried out in a beaker (250 mL) with H_2O_2 (100 mM, 0.31 wt.%) and catalyst (0.05–0.3 g L^{-1}). At a time interval, a solution sample (1 mL) was passed through a polyether sulfone filter (0.22 µm) and diluted into a 100 mL volumetric flask. Then 3 mL sample was added into 0.5 mL mixed solution (0.05 M $C_4K_2O_9Ti$ and 3 M H_2SO_4). The solution samples were analyzed at 390 nm on a spectrophotometer (Agilent Technologies, Cary Series).[26]

Supporting Information

Supporting Information is available from the Wiley Online Library or from the author.

Acknowledgements

The authors acknowledged the help from the analytical lab in the School of Chemical Engineering at The University of Adelaide. This work was supported by the Australian Research Council (DP200103206 and DE210100253).

Open access publishing facilitated by The University of Adelaide, as part of the Wiley - The University of Adelaide agreement via the Council of Australian University Librarians.

Conflict of Interest

The authors declare no conflict of interest.

Data Availability Statement

The data that support the findings of this study are available from the corresponding author upon reasonable request.

Keywords

catalytic polymerization, dual-asymmetric MnO_2 nanotubes, H_2O_2 decomposition, microreactors, peroxymonosulfate

Received: May 6, 2023
Revised: June 20, 2023
Published online:

[1] a) F. Zhang, R. Mundaca-Uribe, N. Askarinam, Z. Li, W. Gao, L. Zhang, J. Wang, *Adv. Mater.* **2022**, *34*, 2107177; b) Y. Yang, K. Hu, P. Zhang, P. Zhou, X. Duan, H. Sun, S. Wang, *Small* **2021**, *17*, 2100927.
[2] M. You, C. Chen, L. Xu, F. Mou, J. Guan, *Acc. Chem. Res.* **2018**, *51*, 3006.
[3] F. Novotný, H. Wang, M. Pumera, *Chem* **2020**, *6*, 867.
[4] K. Villa, F. Novotný, J. Zelenka, M. P. Browne, T. s. Ruml, M. Pumera, *ACS Nano* **2019**, *13*, 8135.
[5] W. Z. Teo, R. Zboril, I. Medrik, M. Pumera, *Chem. - Eur. J.* **2016**, *22*, 4789.
[6] X. Duan, H. Sun, S. Wang, *Acc. Chem. Res.* **2018**, *51*, 678.
[7] a) C. Wang, S. Jia, Y. Zhang, Y. Nian, Y. Wang, Y. Han, Y. Liu, H. Ren, S. Wu, K. Yao, *Appl Catal B* **2020**, *270*, 118819; b) L. Liu, Q. Liu, Y. Wang, J. Huang, W. Wang, L. Duan, X. Yang, X. Yu, X. Han, N. Liu, *Appl Catal B* **2019**, *254*, 166; c) X.-C. Zhang, S.-H. Wu, S.-Y. Jia, C. Wang, S.-W. Sun, X.-M. Wang, Z.-H. Meng, Y.-Y. Lin, Y. Liu, H.-T. Ren, *Chem. Eng. J.* **2020**, *397*, 125351; d) C. Wang, S.-Y. Jia, Y. Han, Y. Li, Y. Liu, H.-T. Ren, S.-H. Wu, X. Han, *ACS EST Engg.* **2021**, *1*, 1275; e) Y. Yang, P. Zhang, K. Hu, P. Zhou, Y. Wang, A. H. Asif, X. Duan, H. Sun, S. Wang, *Appl Catal B* **2022**, *315*, 121593.
[8] Y. Yang, W. Ren, K. Hu, P. Zhang, Y. Wang, X. Duan, H. Sun, S. Wang, *Chem Catal* **2022**, *2*, 1858.
[9] R. S. Ribeiro, A. M. Silva, J. L. Figueiredo, J. L. Faria, H. T. Gomes, *Carbon* **2013**, *62*, 97.
[10] J. Luo, H. Zhu, H. Fan, J. Liang, H. Shi, G. Rao, J. Li, Z. Du, Z. Shen, *J Phys Chem* **2008**, *112*, 12594.
[11] J. Huang, H. Zhang, *Environ Int* **2019**, *133*, 105141.
[12] A. T. Stone, *Environ. Sci. Technol.* **1987**, *21*, 979.
[13] E. C. Gentry, R. R. Knowles, *Acc. Chem. Res.* **2016**, *49*, 1546.
[14] B.-T. Zhang, W. Xiang, X. Jiang, Y. Zhang, Y. Teng, *J. Environ. Eng.* **2016**, *142*, 04016003.
[15] a) N. Shaikh, S. Taujale, H. Zhang, K. Artyushkova, A.-M. S. Ali, J. M. Cerrato, *Environ. Sci. Technol.* **2016**, *50*, 10978; b) S. Balgooyen, P. J. Alaimo, C. K. Remucal, M. Ginder-Vogel, *Environ. Sci. Technol.* **2017**, *51*, 6053.
[16] a) D. Rao, J. Chen, H. Dong, J. Qiao, B. Zhou, Y. Sun, X. Guan, *Water Res.* **2021**, *188*, 116481; b) S. Ndayiragije, Y. Zhang, Y. Zhou, Z. Song, N. Wang, T. Majima, L. Zhu, *Appl Catal B* **2022**, *307*, 121168.
[17] W. Ren, L. Xiong, G. Nie, H. Zhang, X. Duan, S. Wang, *Environ. Sci. Technol.* **2019**, *54*, 1267.
[18] Y. Yang, P. Zhang, K. Hu, X. Duan, Y. Ren, H. Sun, S. Wang, *Appl Catal B* **2021**, *286*, 119903.
[19] T. Zhang, Y. Chen, Y. Wang, J. L.e Roux, Y. Yang, J.-P. Croué, *Environ. Sci. Technol.* **2014**, *48*, 5868.
[20] Y.-J. Zhang, G.-X. Huang, L. R. Winter, J.-J. Chen, L. Tian, S.-C. Mei, Z. Zhang, F. Chen, Z.-Y. Guo, R. Ji, *Nat. Commun.* **2022**, *13*, 3005.
[21] L. Bellamy, *The infra-red spectra of complex molecules*, Springer Science & Business Media, xx **2013**.
[22] B. M. Molloy, D. K. Hyslop, J. S. Parent, *Polym. Eng. Sci.* **2014**, *54*, 2645.
[23] J. Huang, Y. Dai, K. Singewald, C.-C. Liu, S. Saxena, H. Zhang, *Chem. Eng. J.* **2019**, *370*, 906.
[24] a) A. Reyhani, T. G. McKenzie, Q. Fu, G. G. Qiao, *Macromol. Rapid Commun.* **2019**, *40*, 1900220; b) Z.-Q. Liu, S.-Q. Yang, H.-H. Lai, C.-J. Fan, Y.-H. Cui, *Water Res.* **2022**, *221*, 118769.
[25] Z. B. Jildeh, J. Oberländer, P. Kirchner, P. H. Wagner, M. J. Schöning, *Nanomaterials* **2018**, *8*, 262.
[26] S. Zhong, Z.-S. Zhu, P. Zhou, L. Shi, X. Duan, B. Lai, S. Wang, *ACS Appl. Nano Mater.* **2022**, *5*, 12095.

